

Macromolecular crowding tuned extracellular matrix deposition in a bioprinted human rhabdomyosarcoma model

 The corrections made in this section will be reviewed and approved by a journal production editor.

Stefania D'Agostino^{a,b}, Markus Rimann^c, Piergiorgio Gamba Piergiorgio^a, Giorgio Perilongo^a, Michela Pozzobon^{a,b,**}, michela.pozzobon@unipd.it, Michael Raghunath^{c,*}, ragh@zhaw.ch

^aDepartment of Women's and Children's Health, University of Padova, Italy

^bStem Cells and Regenerative Medicine Laboratory, Institute of Pediatric Research (IRP) Città della Speranza, Padova, Italy

^cInstitute of Chemistry and Biotechnology, Center for Cell Biology and Tissue Engineering, Zurich University of Applied Sciences (ZHAW), Wädenswil, Switzerland

*Corresponding author.

**Corresponding author. Department of Women's and Children's Health, University of Padova, Italy.

Abstract

The role of the extracellular matrix (ECM) in tumor recurrence and metastasis has been gaining attention. Indeed, not only cellular, but also structural proteins influence migratory and invasive capacity of tumor cells, including growth and resistance to drugs. Therefore, new *in vitro* tumor models that entail improved ECM formation and deposition are needed. Here, we developed three-dimensional (3D) models of pediatric soft tissue sarcoma (Rhabdomyosarcoma [RMS]) with the two major subgroups, the embryonal (ERMS) and the alveolar (ARMS) form. We applied macromolecular crowding (MMC) technology to monolayer cultures, spheroids, and 3D bioprinted constructs. In all culture models, exposure to MMC significantly increased ECM deposition. Interestingly, bioprinted constructs showed a collagen and fibronectin matrix architecture that was comparable to that of tumor xenografts. Furthermore, the bioprinted model not only showed tumor cell growth inside the structure but also displayed cell clusters leaving the edges of the bioprinted construct, probably emulating a metastatic mechanism. ARMS and ERMS cells reacted differently in the bioprinted structure. Indeed, the characteristic metastatic behavior was much more pronounced in the more aggressive ARMS subtype. This promising approach opens new avenues for studying RMS microenvironment and creating a platform for cancer drug testing including the native tumor ECM.

Keywords:

Bioprinting, Rhabdomyosarcoma microenvironment, Macromolecular crowding, 3D model of rhabdomyosarcoma

Abbreviations

No keyword abbreviations are available

©2022 This manuscript version is made available under the CC-BY-NC-ND 4.0 license <https://creativecommons.org/licenses/by-nc-nd/4.0/>

You may find the published version: Stefania D'Agostino, Markus Rimann, Piergiorgio Gamba, Giorgio Perilongo, Michela Pozzobon, Michael Raghunath, Macromolecular crowding tuned extracellular matrix deposition in a bioprinted human rhabdomyosarcoma model, *Bioprinting*, 27(2022)e00213, <https://doi.org/10.1016/j.bprint.2022.e00213>

Abbreviations

ARMS alveolar rhabdomyosarcoma

BSA bovine serum albumin

COLI collagen I
COLIV collagen IV
COLVI collagen VI
DAPI 4',6-diamidino-2-phenylindole
DMEM Dulbecco's Modified Eagle Medium
ECM extracellular matrix
ERMS embryonal rhabdomyosarcoma
FBS fetal bovine serum
FN fibronectin
IF immunofluorescence
LAM laminin
MFI mean fluorescence intensity
MMC macromolecular crowding
MMP2 metalloprotease 2
PFA paraformaldehyde
RMS rhabdomyosarcoma

TME tumor microenvironment.

1 Introduction


The tumor microenvironment (TME) plays a crucial role in cancer recurrence and metastatic behavior [1]. The TME composition consider both the cell compartment, such as the immune cells, the stromal and endothelial cells, and the protein compartment. Most of the studies on TME carried out in adulthood cancers of epithelial origin [2]; highlighted the role of crosstalk between transformed cells and their niche, linking altered ECM composition with neoplasm pathology [3]. Pediatric soft-tissue tumors are a leading cause of disease-associated deaths in children. The study of their TME is now in his infancy mainly because pediatric sarcoma are rare pathologies of mesenchymal origin and the cancer cells are the cell type more represented cell type, with almost total absence of immune and stromal cells [4,5].

Rhabdomyosarcoma (RMS) is among the most prevalent and aggressive tumors that develop during childhood, specifically in skeletal muscle tissue or in hollow organs such as the bladder or uterus [6]. The two most frequent variants are embryonal RMS (ERMS) and alveolar RMS (ARMS). The latter is the more aggressive with a strong metastatic tendency. The development of a more personalized therapy with focus on the ECM composition instead of cancer cells can be a new strategy to strengthen in order to increase the survival rates for patients and in particular for children with ARMS. However, primary tumor samples from RMS patients are scarce and, in most cases, oncological scientists have access only to metastatic tumor material after the first round of chemotherapy. Therefore, a combination of innovative tissue engineering approaches; and cellular and molecular biology expertise is needed to make headways in building three-dimensional (3D) models that could recapitulate the tumor tissue and its ECM composition. While this strategy has already been pursued particularly for epithelial tumors by creating tumor spheroids [7] and organoids [8], it has not yet been applied for soft tissue tumors, in particular RMS. Moreover, recent findings in ECM composition of RMS [4,9], stimulate the development of new *in vitro* 3D models of this tumor [4,10]. In native tissues, ECM is produced mainly by fibroblasts and the deposition of highly crowded/dense macromolecules in the extracellular space is achieved, leading to a highly volume-occupied or crowded solution [11,12].

Nowadays, this effect, called macromolecular crowding (MMC), is successfully applied in tissue engineering, whereby the addition of carbohydrate-based polymers to culture medium [11], facilitates *in vitro* deposition of ECM and thus the formation of a pericellular matrix [13]. Besides MMC treatment to recreate a 3D physiological microenvironment in monolayer culture, the bioprinting technology has proven to be a very promising tool to recapitulate the inherent 3D tissue architecture [14]. The technology allows depositing cells, scaffolding material, and bioactive molecules in predefined 3D structures to emulate native tissue environment [15,16]. The scaffolding material called "bioink", better specified as "biomaterial ink" [17] in the context of bioprinting, is an ECM substitute. Different bioinks are currently in use and most of them are derived from natural biopolymers, such as alginate, chitosan, hyaluronic acid, fibrin, gelatin-(methacryloyl), collagen I, Matrigel® [18]. The most common bioprinting technologies include laser-assisted-, inkjet- and extrusion-bioprinting. We have been using a micro valve-based inkjet bioprinting technology to generate skin tissue models and muscle-tendon tissues with primary cells [19,20]. Recently, we have printed functional human skeletal muscle tissues [21]. Human skeletal muscle precursor cells were mixed with Matrigel® and printed in droplets to produce a dumbbell shape that was fixed with posts allowing myotube formation. The differentiated muscle tissue was contracting after electrical stimulation and showed increased muscle force after caffeine and Tirasentif treatment [21].

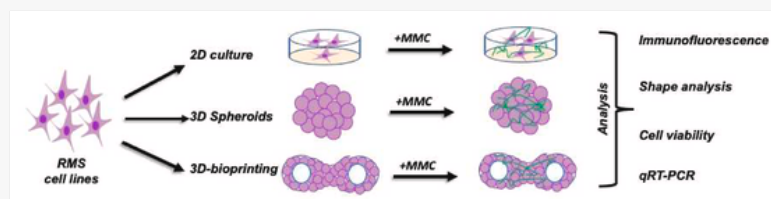
In the present work, we first applied MMC as facilitator of ECM deposition in RMS cell lines in monolayer culture, then in spheroid format, and finally combined it with bioprinting technology as developed in Ref. [21] (Fig. 1). The latter strategy allowed the creation of a 3D *in vitro* RMS model that demonstrated ECM deposition similar to xenotransplanted RMS cells into immunodeficient mice and showed shedding of cell clusters, indicating an *in vitro*

metastasis-like process. This combined approach will be useful to explore new possibilities for precision medicine in pediatric RMS.

 Images are optimised for fast web viewing. Click on the image to view the original version.

alt-text: Fig. 1

Fig. 1



The outline of the work is depicted. Rhabdomyosarcoma (RMS) cell lines (RH30 for ARMS and RD for ERMS variant) have been tested with macromolecular crowding (MMC) in 3 different conditions: in flat two-dimensional (2D) culture, in spheroids (3D) and in 3 dimensional (3D) bioprinted shape. Analyses have been performed after MMC treatment according to the following time points: 5 days for the 2D, 10 days for the spheroid conditions and 21 days for the 3D bioprinted model.

2 Materials and methods

2.1 Cell lines

The RH30 (ARMS) and RD (ERMS) cell lines, were kindly provided by the Solid Tumors laboratory (Prof. Bisogno, Padova, Italy). All cell lines were cultured in high glucose Dulbecco's Modified Eagle Medium (DMEM), supplemented with 10% fetal bovine serum (FBS) 1% penicillin/streptomycin, 1% L-glutamine (all reagents were from Gibco, Dublin, Ireland) in tissue culture flasks (Sarstedt, Nümbrecht, Germany) at 37 °C, 5% CO₂ and 95% relative humidity.

For MMC stimulation, 7×10^5 RH30 or RD cells/well were seeded in a 24-well plate, and after 24 h 37.5 g/L Ficoll 70, 25 g/L Ficoll 400 (both from GE Healthcare, Chicago, USA) and 0,1 mM L-ascorbic acid (Sigma-Aldrich, Saint Louis, USA) were added to the culture medium. Cells were fixed and analyzed after 5 days incubation at 37 °C, 5% CO₂ and 95% relative humidity.

2.2 Xenograft

In order to have tissue samples as control for ECM protein expression, samples from xenografts were obtained as previously described [4]. Briefly, twelve-week-old male and female mice (C; 129S4-Rag2tm1.Flv Il2rgtm1.Flv/J, also called Rag2^{-/-}γc^{-/-}) were used as recipients for subcutaneous flank injections of 2×10^6 human RMS cells (RH30 and RD) resuspended in Matrigel® (Corning, New York, USA). Mice injected with 2×10^6 RH30 cells mimicked the ARMS variant, while mice injected with 2×10^6 RD cells mimicked the ERMS variant. The treatments were approved by the institutional animal care and use committee (CEASA, protocol 304/2017) and were communicated to the Ministry of Health and local authorities in accordance with Italian Law (DL n. 16/92 art. 5). Xenogenic samples (4 samples for each tumor) were harvested 21 days post injection.

2.3 Spheroids 3D model

The RH30 (ARMS) and RD (ERMS) spheroids were formed by seeding 5×10^3 cells in ultralow-adhesion (ULA), round-bottom 96-well plates (Corning, New York, USA) in low glucose DMEM supplemented with B27 (both from Gibco, Dublin, Ireland), 10 ng/mL bFGF and 20 ng/mL EGF (both from ORFGenetics, Kopavogur, Iceland).

For macromolecular crowding (MMC), 37.5 g/L 70 kDa Ficoll, 25 g/L 400 kDa Ficoll and 0.1 mM L-ascorbic acid were added to the culture medium on the day of cell seeding, and spheroids were cultured for 10 days. On day 10, either spheroids were fixed and processed for IF as described above, or brightfield and phase contrast images were taken at 10X magnification with OlympusIX81 (Olympus corporation, Tokyo, Japan) microscope and processed for shape parameters detection using Fiji software. Alternatively, a pool of 6 spheroids was stored snap frozen in liquid nitrogen for RNA extraction and qRT-PCR analyses (see below).

2.4 Immunofluorescence


Xenogenic samples harvested from mice, 3D bioprinted constructs and tumor spheroids were fixed for 1 h in 4% PFA and included in Killik cryostat embedding medium (both from Bio-Optica, Milano, Italy). Four different experiments

for each condition were performed and analyzed. All the samples were stored at -80°C until they were cut in $7\ \mu\text{m}$ slices using Leica CM1520 cryostat (Leica Microsystems, Wetzlar, Germany).

For immunofluorescence (IF) analyses, cryosections were permeabilized with 0.5% Triton X-100 (Bio-Rad, Hercules, USA) and then incubated with 10% horse serum (Gibco, Dublin, Ireland), primary antibodies and later with secondary Alexa Fluor-conjugated antibodies, both resuspended in 1% bovine serum albumin (BSA, Sigma-Aldrich, Saint Louis, USA). The antibodies used are listed in [Table 1](#). Nuclei were counterstained with fluorescent mounting medium with 100 ng/mL 4',6-diamidino-2-phenylindole (DAPI) (Sigma-Aldrich, Saint Louis, USA). Each glass slide was prepared carrying 10 tissue slices obtained cutting the whole sample, from the border to the center. For each count performed, 10 random pictures at 20X magnification, were collected using [LeicaDM16000B](#)/[Olympus IX81](#) microscope ([Olympus/Leica Microsystems, Tokyo/Wetzlar, Japan/Germany](#)), and the quantification of the positive area or the mean fluorescence intensity (MFI) were analyzed using Fiji software [22] using the shape descriptors here described [23]; [circularity](#), [area](#), [perimeter](#), roundness [and](#) solidity. MFI is defined as the sum of the values of all the pixels in the region of interest divided by the number of pixels.

alt-text: Table 1

Table 1

 The table layout displayed in this section is not how it will appear in the final version. The representation below is solely purposed for providing corrections to the table. To preview the actual presentation of the table, please view the Proof.


Immunofluorescence antibody list.

Antibodies- Company	Dilution	Incubation time
Mouse anti-fibronectin (Invitrogen, Carlsbad, USA) (RRID: AB_10982280)	1:100	Overnight at 4°C
Rabbit anti-laminin (Sigma-Aldrich, Saint Louis, USA) (RRID: AB_477163)	1:200	1 h at 37°C
Rabbit anti-Collagen I (Thermo Fisher Scientific, Waltham, USA) (RRID: AB_2552689)	1:80	Overnight at 4°C
Mouse anti-Collagen III (Abcam, Cambridge, UK) (RRID: AB_305413)	1:100	1 h at 37°C
Rabbit anti- Collagen IV (Abcam, Cambridge, UK) (RRID: AB_305584)	1:100	1 h at 37°C
Rabbit anti-Collagen VI (Abcam, Cambridge, UK) (RRID: AB_305585)	1:100	1 h at 37°C
Mouse anti-MMP2 (Millipore, Burlington, USA) (RRID: AB_11215101)	1:100	1 h at 37°C
Goat anti-Mouse IgG Secondary Antibody, Alexa Fluor 488 (Invitrogen, Carlsbad, USA) (RRID: AB_2534069)	1:200	1 h at 37°C
Chicken anti-Rabbit IgG Secondary Antibody, Alexa Fluor 488 (Invitrogen, Carlsbad, USA) (RRID: AB_141735)	1:200	1 h at 37°C
Goat anti-Mouse IgG Secondary Antibody, Alexa Fluor 594 (Invitrogen, Carlsbad, USA) (RRID: AB_141372)	1:200	1 h at 37°C
Chicken anti-Rabbit IgG Secondary Antibody, Alexa Fluor 594 (Invitrogen, Carlsbad, USA) (RRID: AB_141840)	1:200	1 h at 37°C

2D cultured cells were also fixed for 1 h in 4% PFA before IF staining was carried out the same way as for frozen tissue sections. Nuclei were counterstained using Hoechst [33342](#) (Agilent, Santa Clara, USA).

2.5 Gene expression analysis (qRT-PCR)

Total RNA was extracted from monolayer cultures, xenotransplants, spheroids- and 3D-bioprinted samples-derived cells using RNeasy Plus Mini kit (Qiagen, Hilden, Germany) or Trizol reagent (Life Technologies, Carlsbad, USA) following the manufacturer's instructions. RNA was quantified with a ND-2000 spectrophotometer. For all samples total RNA was reverse transcribed with SuperScript II (Life Technologies, Carlsbad, USA), following supplier's instructions. Real Time PCR was performed using a Vii7 Real-Time PCR System (Applied Biosystem, Foster City, USA); reactions were carried out in triplicates using SYBR Green master mix (Applied Biosystem, Foster City, USA). A relative quantification (RQ) was calculated by $\Delta\Delta\text{Ct}$ method using a software implemented in Vii7 Real-Time PCR System. GAPDH was used as reference (or "housekeeping") gene for normalization, based on its constant expression in all the 2D and 3D human and murine samples used (less than two PCR cycles difference in expression among the different samples). Fetal skeletal muscle or HT29 cells were used for calibration. For each quantification, a confidence interval (CI) of 95% was calculated. Primer sequences used are listed in [Table 2](#).

 The table layout displayed in this section is not how it will appear in the final version. The representation below is solely purposed for providing corrections to the table. To preview the actual presentation of the table, please view the Proof.

Primer list.

GENE	SEQUENCE	T _m	NM
GAPDH-F	TCCTCTGACTTCAACAGCGA	60 °C	NM_001256799.3
GAPDH-R	GGGTCTTACTCCTTGGAGGC		
FN1-F	GAAGACATACCACGTAGGAGAACA	57 °C	NM_001306129.2
FN1-R	AGGTCTGCGGCAGTTGTC		
MMP2-F	CTCATCGCAGATGCCTGGAA	60 °C	NM_001127891.2
MMP2-R	TTCAGGTAATAGGCACCCTGAAGA		
FBN1-F	GAAGGTGCCAAGATTTGCGA	59 °C	NM_0001385
FBN1-R	AGCATTCCTGCTTGGAGTGA		
COL6A1-F	GCCCAGATCTGCATAGACAAGA	59 °C	NM_001844.5
COL6A1-R	CGTTGGTGGTGTCAAAGTT		
COL1A1-F	AGCAAGAACCCCAAGGACAA	59 °C	NM_000088.4
COL1A1-R	TACTCGAACTGGAATCCATCGG		
CXCR4-F	CTCAGCGTCTCAGTGCCCTT	60 °C	NM_001008540.2
CXCR4-R	AATCCTACAACCTCTCCTCCCA		

2.6 3D bioprinting

RH30 and RD 3D bioprinted constructs were created with a RegenHU 3DDiscovery bioprinter. Four experiments with 3 replicates for each condition were assessed. The protocol was adopted from Ref. [20] for RMS cells, using a dumbbell-shaped template of 8 mm in length designed with BioCAD software [20]. Firstly, the bottom of wells (15 mm diameter) of a 24-well plate was covered with 1 mL 0.8% agarose (Sigma Aldrich, Saint Louis, USA) dissolved in high glucose DMEM, and was allowed to solidify and to serve as a foundation (layer) to print on. RMS cells were suspended in Matrigel® at a density of 2×10^7 cells/mL and loaded into a 3 mL printing cartridge and kept at a temperature below 6 °C throughout the printing process. The constructs were printed using a jetting microvalve with a diameter of 0.150 mm, with a valve opening time of 200 μ s and a pressure of 55 kPa. 4 identical layers were printed on top of each other with a 2-min incubation time between the layers, to ensure complete polymerization of the layers. The final volume of cell suspension deposited for each model was 50 μ L. Subsequently, two 1 mm posts were vertically inserted at 8 mm distance to pin each dumbbell end to the agarose layer. Then the plate was incubated for 15 min at 37 °C before culture medium addition. For MMC exposure, 24 h after printing, the medium was switched to medium containing 37.5 g/L Ficoll 70, 25 g/L Ficoll 400 and 0.1 mM L-ascorbic acid. Viability of bioprinted constructs was monitored up to 21 days with Presto Blue (Invitrogen, Carlsbad, USA) and emitted fluorescence was quantified using a FLUOstar OPTIMA fluorimeter (BMG Labtech, Ortenberg, Germany). After 21 days constructs were either stored snap frozen for qRT-PCR analyses or processed for IF as stated above.

2.7 Statistical analysis

All graphs, data normality test and all statistical tests were produced with GraphPad software 6. Data are expressed as means \pm SD. To compare two groups, statistical significance was determined using an equal-variance Student's *t*-test for normal data set or Mann-Whitney *U* test for non-normal data. The non-parametric Kruskal-Wallis One-Way ANOVA test for data non-normally distributed was applied to compare more than 2 groups. A *p* value below 0.05 was considered to be statistically significant. Legend: * = *p* < 0.05; ** = *p* < 0.01; *** = *p* < 0.001; **** = *p* < 0.0001.

3 Results

3.1 MMC treatment with 2D culture

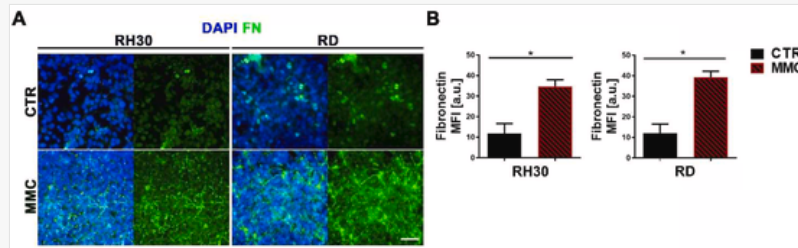
In the first round of experiments, ascorbic acid and MMC treatment were applied on monolayer cultures of RH30 (ARMS) and RD (ERMS) cells to test their effects on ECM deposition. While control RH30 cultures showed some

fibronectin-positive stipples, treated samples displayed a fine extracellular meshwork of fibronectin matrix in both tumor types (N = 4 for each cell line. Fig. 2 A, B). A comparable reticular fibronectin pattern was present in xenograft biopsies (N = 4 for ARMS xeno, N = 4 for ERMS xeno. Fig. S1). These results prompted us to explore MMC treatment on RMS spheroids and bioprinted 3D constructs.

i Images are optimised for fast web viewing. Click on the image to view the original version.

alt-text: Fig. 2

Fig. 2



Macromolecular crowding effect on monolayer cultures of RH30 (left) and RD (right). A IF staining for fibronectin in the control cultures (CTR) and under MMC for both cell types. The left panels show the overlay of DAPI (cell nuclei; blue) and fibronectin (FN, green), and the right panel represents FN-staining only. Scale bar = 50 μ m. B Mean fluorescence intensity (MFI) was measured for fibronectin staining in monolayer cultures of RH30 and RD with or without MMC treatment. N = 4, non parametric Mann-Whitney test * $p < 0.05$. (For interpretation of the references to colour in this figure legend, the reader is referred to the Web version of this article.)

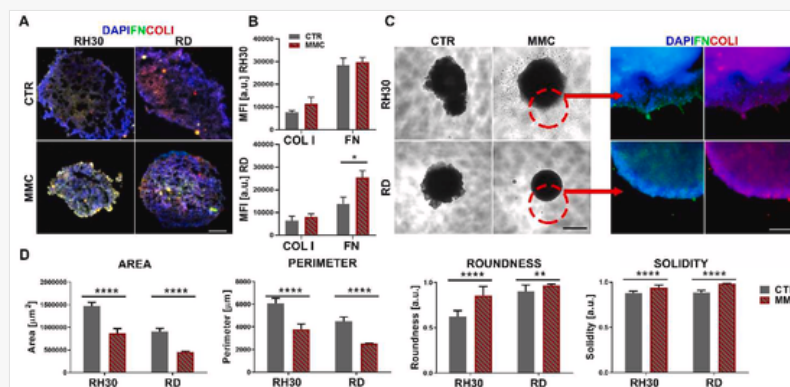
3.2 MMC treatment of spheroids 3D model

In order to explore the ECM-amplifying effects of MMC treatment in a 3D environment represented by high tumor cell density, the Ficoll cocktail was applied to spheroid cultures of RH30 (ARMS) and RD (ERMS) cells (N = 12 spheroids for each cell line). IF staining of spheroids for collagen I and fibronectin highlighted that in this model of closely-packed cells together, the MMC treatment do not modify the already strong production of ECM. Indeed, the difference in protein production of treated and untreated spheroids was not significant, except in fibronectin expression of RD cells (Fig. 3A and B). However, MMC treated spheroids were more compact, smaller and with higher roundness 10 days post MMC administration (Fig. 3C and D). In addition, after 5 days culture, some RH30 cells started adhering to the bottom of the well only in presence of MMC, although not compromising the formation of the spheroids (Fig. 3C). Of note, the attached cells deposited fibronectin and collagen I, which favored adhesion to the well bottom (Fig. 3C, right). In summary, all these findings underlined that MMC stimulated ECM protein deposition leading to spheroid attachment and cell interaction with the surrounding environment, in some instances even overriding a non-adherent coating.

i Images are optimised for fast web viewing. Click on the image to view the original version.

alt-text: Fig. 3


Fig. 3



MMC effect on RH30 and RD spheroids. A IF staining for fibronectin (FN; green) and collagen I (COLI; red) on RH30 -ARMS- (left) and RD -ERMS- (right) spheroids frozen sections in absence or presence of MMC treatment (DAPI, cell nuclei; blue), scale bar = 50 μm . **B** Mean fluorescence intensity (MFI) of collagen I and fibronectin expression in spheroid cryosections. **C** Left. Phase contrast images of the spheroids seeded in ULA plates in all the tested conditions, and detail of RH30 adhered cells at the bottom of the well. Scale bar = 200 μm **Right.** IF staining of fibronectin and collagen I in RH30 and RD spheroids treated with MMC showing the presence of adhered cells below the RH30 spheroid. Scale bar = 50 μm . **D** Quantification of shape parameters of RH30 and RD spheroids (area, perimeter, roundness, and solidity) without and with MMC treatment, N = 12, Student's *t*-test **p* < 0.05, ***p* < 0.01, ****p* < 0.0001. (For interpretation of the references to colour in this figure legend, the reader is referred to the Web version of this article.)

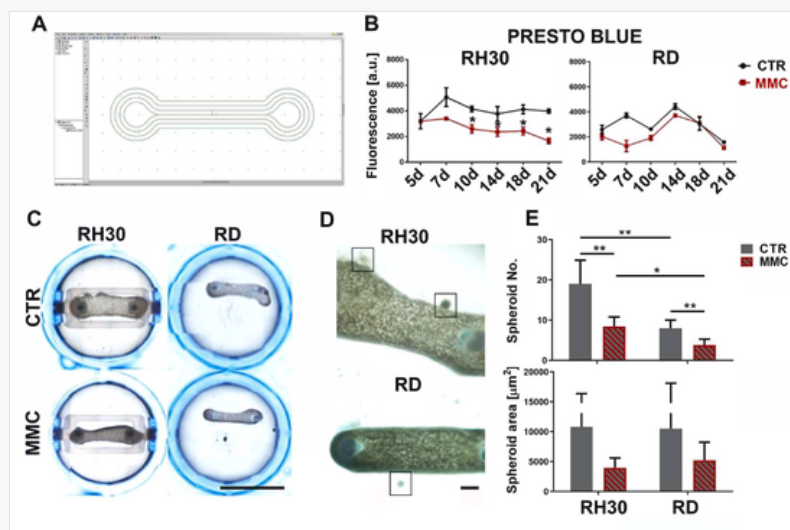
3.3 MMC with bioprinted construct

Finally, we used a 3D bioprinting strategy that has been shown to recapitulate the spatially organized muscle tissue architecture. According to our previous work [21], we could demonstrate that initially printed dumbbell structures developed into parallel aligned myofibers over time, reflecting the native muscle tissue morphology as it has been demonstrated by Atala [24]. The bioprinted model resembled the morphology of healthy human muscle in which RMS usually develops [20,25]. Dumbbell-shaped constructs of RH30 (ARMS) or RD (ERMS) cells suspended in Matrigel® were printed and cell viability was confirmed after monitoring for 21 days (N = 6 for each cell line. Fig. 4A and B). 24 h after printing, culture medium was changed and MMC was applied with media exchange every 48 h. Noticeably, the addition of MMC resulted in more compact constructs compared to untreated conditions, and this was true for both cell lines (Fig. 4C).

 Images are optimised for fast web viewing. Click on the image to view the original version.

alt-text: Fig. 4

Fig. 4




3D bioprinted RMS samples and spheroid release. **A.** The dumbbell-shaped template used to print cells is depicted. **B** Cell viability assessment of bioprinted RH30 (ARMS) (left) and RD (ERMS) (right) constructs until 21 days after printing. **p* < 0.05 **C.** Brightfield images of MMC-treated (MMC) and untreated (CTR) RH30 (ARMS) and RD (ERMS) 3D bioprinted samples (day 21). Some of the released spheroids are visible. Scale bar: 10 mm **D.** Representative pictures of spheroids before MMC stimulation. Brightfield image showing spheroid release from the central body of the bioprinted models of RH30 (top) and RD cells (bottom), 10d after culture. Scale bar: 1 mm. **E.** Number of released spheroids (Spheroid No.) on day 10 after printing (top) and quantification of spheroid dimension (Spheroid area, bottom). N = 6, Mann-Whitney test **p* < 0.05, ***p* < 0.01.

Initially, without MMC, the cells were homogeneously distributed throughout the printed construct. However, over time cells moved within the Matrigel® and redistributed to the surface of the dumbbell shapes. In some surface areas, high cell density led to cell aggregate formation that clearly resembled spheroids (Fig. 4D). From day 10 of culture cell aggregates detached from the construct, and were collected during medium change; in parallel, fluorescent cell viability measurement in media supernatant with Presto Blue, indicated that cell viability significantly diminished in RH30 samples after MMC (Fig. 4B) but this did not happen in RD samples. The progressive detachment of cell aggregates indicates that cells were migrating outside the bioprinted construct.

Under MMC conditions, more assembled ECM deposits were evident, and cells were more evenly distributed throughout the construct. Also bioprinted Matrigel® MMC treated embedded with RH30 and RD cells, respectively,

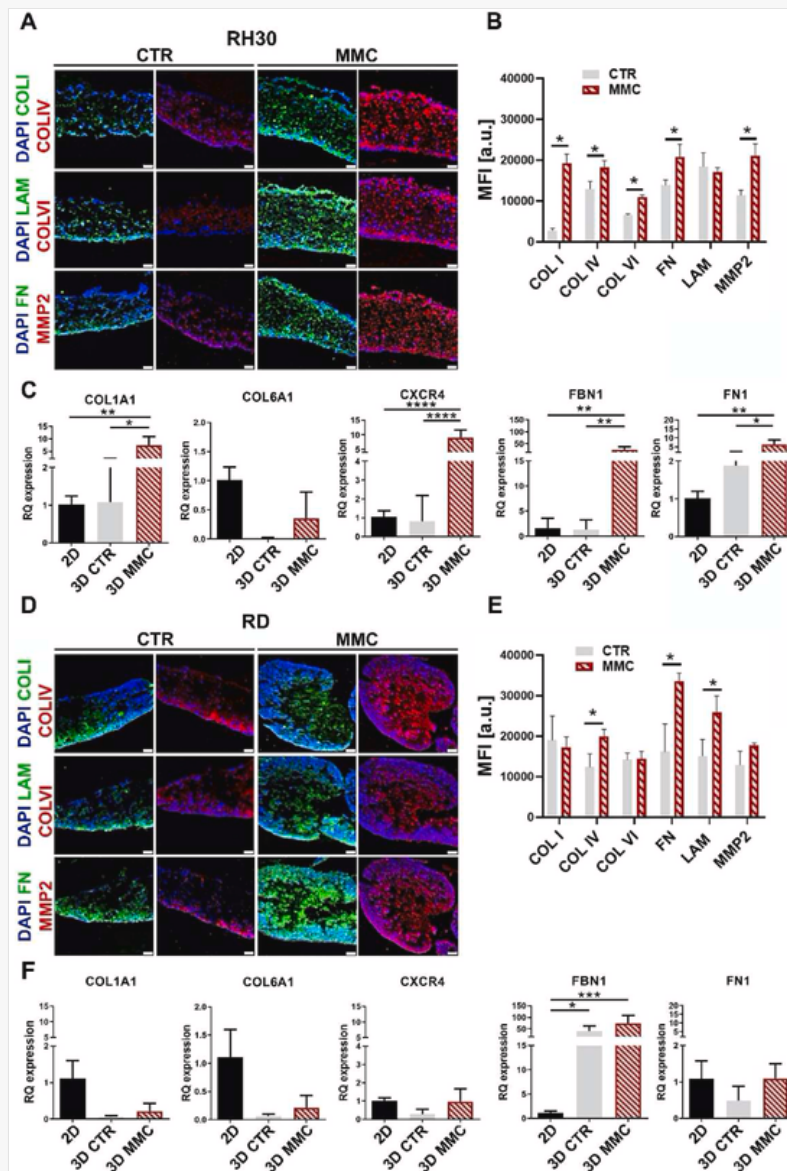
give rise to shedding spheroids (of about $5 \times 10^5 \mu\text{m}^2$ surface area) and the number and size of spheroids was higher in RH30 compared to RD (Fig. 4D and E). In all, the MMC treated conditions produced less and smaller spheroids in comparison with the untreated ones.

Collagen I, Laminin and Fibronectin deposition was more pronounced in the MMC treated samples compared to the untreated controls. Indeed, this was confirmed in a significant manner, on RH30 samples and, to a lesser extent, on RD samples (Fig. 5A, B, D, E). These findings in protein expression of bioprinted samples demonstrated the similarity to a native RMS tissue (Fig. S1). In gene expression analysis, the ECM proteins FBN1, COL1A1 and FN1 were upregulated in the RH30 MMC treated 3D-printed samples and not in RD MMC treated 3D-printed samples, as well as CXCR4, **the receptor of SDF1, involved in the recruitment of RMS cells to bone marrow to form metastases**, was significantly increased (N = 4 for each cell line. Fig. 5C, F). These results highlighted the effect of MMC treatment on the enhancement of ECM components production and on different ECM assembly and consistency on RH30 samples.

 Images are optimised for fast web viewing. Click on the image to view the original version.

alt-text: Fig. 5

Fig. 5



Characterization of 3D bioprinted RMS samples. A. IF staining of fibronectin (FN), collagen I (COLI), collagen IV (COLIV), collagen VI (COLVI), laminin (LAM) and MMP2 in bioprinted RH30 constructs without (**left**) and with (**right**) MMC treatment at 21 days. Cell nuclei were counterstained with DAPI. Scale bar = 50 μm . B. Mean fluorescence intensity (MFI) measurements of 3D bioprinted RH30 samples at day 21. C. Gene expression analysis of FBN1, COL6A1, COL1A1, CXCR4, and FN1 on monolayer culture (2D) and 3D bioprinted samples of RH30 with and without MMC treatment. 2D cells are used as control. D. IF staining of FN, COLI, COLIV, COLVI, LAM and MMP2 in bioprinted RD constructs without (**left**) and with (**right**) MMC treatment at 21 days. Cell nuclei were counterstained with DAPI. Scale bar = 50 μm . E. Mean fluorescence intensity (MFI) measurements of 3D bioprinted RD samples at day 21. F. Gene expression analysis of FBN1, COL6A1, COL1A1, CXCR4, and FN1 on monolayer culture (2D) and 3D bioprinted samples of RD with and without MMC treatment. 2D cells are used as control. N = 4, Kruskal-Wallis One-Way ANOVA test. *p < 0.05, **p < 0.01, ***p < 0.001, ****p < 0.0001.

4 Discussion

The recent development of 3D cell culture systems is a means of recapitulating the natural tissue architecture and microenvironment. Indeed, it is well known that cell behavior varies between 2D monolayer and 3D culture conditions, with differences in cell proliferation, differentiation and gene expression, making 3D cell culture systems a better tool for mirroring *in vivo* cell behavior [26,27].

In this work, we investigated the effect of MMC on RMS cells, cultured in monolayers, 3D spheroids and as 3D bioprinted models to reproduce the complexity of cell-protein interaction.

For this purpose we used two cell lines representing the two most common RMS molecular and histopathological variants: alveolar and embryonal RMS [28–33]. Due to the paucity of human biopsies, the cell lines and the xenogeneic models still the most representative and available to study this pediatric disease [6].

RD cells well represent the embryonic variant (ERMS) [31–33], while the alveolar variant (ARMS), often characterized by the presence of the PAX3/7-FOXO1 fusion protein, is represented by RH30 cells [31,32,34]. The fusion protein is associated with downstream effectors that suppress tumor cell differentiation and improve their growth, motility and invasiveness [35], leading to a worse prognosis and a higher risk of relapse level [36]. With this in mind, we used MMC to stimulate cells to recreate the complexity of protein microenvironment that characterize the invasive behavior of these cancer variants [6]. MMC has been used in combination with ascorbic acid to enhance ECM deposition in mesenchymal cells such as fibroblasts [37,38], tenocytes [39], adipose tissue and bone marrow mesenchymal stromal cells (MSCs) [40,41]. MMC treatment of undifferentiated MSCs leads to enhanced ECM deposition, composed of a variety of collagen types, matricellular proteins, such as laminin and fibronectin, and glycosaminoglycans (e.g. hyaluronic acid) or proteoglycans, like decorin and perlecan, together with ECM remodeling enzymes and their respective inhibitors (LOX, MMP2, TIMP) [11,37–39]. The *de novo* produced intrinsic ECM results in the reorganization of the actin cytoskeleton via the cell adesome [42,43]. Furthermore, a positive feed-back loop is created by enhanced growth factor storage as demonstrated for adipogenesis [40]. Moreover, not only the amount of deposited ECM but also the improved microarchitecture leads to impressive changes in the transcriptome, unleashing a dormant differentiation potential [41], corroborating the concept of dynamic cell-matrix reciprocity, as demonstrated for TME of adulthood pathologies such as breast and colon cancers [44,45].

Nevertheless, apart from a few studies on prostate cancer [46], MMC effect on TME reconstruction and reproduction was not deeply investigated yet. In our study, MMC treatment of tumor cell monolayer cultures resulted in increased production of the glycoprotein fibronectin, not only limited to cell cytoplasm but also deposited in a mesh-like structure outside cells.

To verify this effect in 3D, we first produced tumor spheroids, which have been already used to study RMS extracellular matrix [4,10,47,48]. Spheroids are composed of RMS cells alone and thus lack cell and TME heterogeneity as well as microvasculature. However, these structures mimicked better the tumor microarchitecture compared to flat cultures by adding the important factor of interaction between cells and ECM. RMS cells in spheroids responded to MMC stimulation with increased ECM production and deposition compared to untreated spheroids. The tighter packing of the cells resulted in a more compact and round shaped structure, typical of a stabilized spheroid [26]. In addition, unlike ERMS cells, RH30 spheroids showed a peculiar behavior. For these cells, indeed, MMC acted not only on the migration of the peripheral cells but also on their adhesive properties. The borders of the spheroids disaggregated, while cells adhered to plastic in the ULA plates, displaying the invasive behavior typical of the ARMS variant.

The second 3D RMS model used in this work was bioprinted. This offered the possibility to analyze a larger surface area compared to spheroids (radial shape), as well as a more native morphology that developed after maturation between the two fixing posts, resulting into a longitudinal shape. With the advantage of the fine control over cell and bioink (matrix) deposition, allowing to obtain complex patterns typical of specific organs with high reproducibility, this technique is gaining resonance in the field of tumor modeling [49,50]. To date, very few attempts of building metastases models [51] for sarcoma TME have been made, mainly involving osteosarcoma [52]. Furthermore, the technique has been used to mirror breast cancer and glioblastoma TME including the integration of vascularization [53–56]. To our knowledge this work is the first one reproducing the TME of RMS via 3D bioprinting. The bioink selection is of major concern in order to provide optimal cell compatibility and printability depending on the bioprinting technology used [57]. The optimal bioink must guarantee the balance between printability and biocompatibility [58]. Currently, the bioinks are mainly derived from natural biopolymers and purified ECM because synthetic inks cannot provide the plethora of signals derived by an ECM [59]. Therefore, in our first attempt to build RMS TME, we chose Matrigel®, which is easily printable at low temperatures and contains major basement membrane ECM components [21]. In addition, we treated the model with MMC. In this 3D architecture cells deposited a higher amount of self-produced ECM components in respect to untreated controls.

Building on our earlier work [21], we printed the RMS model in a dumbbell shape with parallel structures to build muscle fiber-like patterns to reproduce the environment where this tumor develops. This offered the possibility to analyze a larger surface area compared to spheroids, as well as a more native morphology (longitudinal rather than radial). After 10 days of culture the newly formed spheroids detached from the central body of the 3D sample, and were lost during medium change, which might be a reason for the apparent decreased metabolic activity as quantified by Presto blue. In the MMC-treated samples, the newly produced ECM imposed some geometrical constraints to cells since they appeared more organized with homogeneous distribution. However, spheroid release persisted with MMC stimulation, mimicking a metastatic process. Interestingly, the number and dimensions of the developed and released spheroids were larger for RH30 compared to RD cells. It is conceivable that this reflects the higher aggressiveness of the alveolar variant of RMS cell line RH30, which leads to a higher degree of metastasis [35], in comparison to the embryonal cell line. qRT-PCR data supported these observations by demonstrating a greater plasticity of the ARMS cells compared to ERMS under MMC treatment. Indeed, in ARMS cells, the MMC stimulation was capable to induce profound changes in the pericellular environment. The genes for ECM constituents, whose remodeling is the first step towards metastasis, were significantly increased, as well as CXCR4, the receptor of SDF1, involved in the recruitment of RMS cells to bone marrow to form metastases [60]. In terms of protein expression, the increased MMP2 expression in MMC-treated samples also confirmed the occurrence of ECM remodeling processes leading to cancer cell migration [61].

5 Conclusion

In conclusion, the novelty of our findings is twofold. Being the first bioprinted model of RMS, the architecture given by 3D bioprinting allowed the production of a 3D model which resembles *ex vivo* RMS samples in morphology. In addition, MMC furnished the stimulus for ECM remodeling, giving a depiction of RMS cell behavior in a 3D microenvironment, from which cells were able to escape, mimicking cell tissue migration. We can argue that the combination of the two elements, MMC and 3D bioprinting, produced a metastasis-like 3D model of RMS suitable for drug development. In the future, cells from patients could be used and our approach opens new therapeutic perspectives in the field of personalized medicine.

CRedit authorship contribution statement

Stefania D'Agostino: Conceptualization, Data curation, Formal analysis, Writing – review & editing. **Markus Rimann:** Conceptualization, Data curation, Formal analysis, Writing – review & editing. **Gamba Piergiorgio:** Funding acquisition. **Giorgio Perilongo:** Funding acquisition. **Michela Pozzobon:** [Conceptualization](#), Data curation, Formal analysis, Writing – review & editing. **Michael Raghunath:** Supervision, Validation.

Declaration of competing interest

The authors declare the following financial interests/personal relationships which may be considered as potential competing interests: Stefania D'Agostino reports financial support was provided by Institute of Pediatric Research Città della Speranza. Michela Pozzobon reports a relationship with University of Padua Department of Women's and Children's Health that includes: employment. None has patent None pending to None. Authors declare no conflict of interest.


Acknowledgments

This research was supported by the [Department of Women and Children Health, University of Padova](#). Stefania D'Agostino is supported by the grant number 21/07 Institute of Pediatric research Città della Speranza (IRP), Italy, PI **02** Michela Pozzobon. The project was initiated and supported through the [EU COST Action CA16119 CellFit](#).

Appendix A Supplementary data

Supplementary data to this article can be found online at <https://doi.org/10.1016/j.bprint.2022.e00213>.

References

 The corrections made in this section will be reviewed and approved by a journal production editor. The newly added/removed references and its citations will be reordered and rearranged by the production team.

[1] M. Ehnman, W. Chaabane, F. Haglund, P. Tsagkozis, The tumor microenvironment of pediatric sarcoma: mesenchymal mechanisms regulating cell migration and metastasis, *Curr. Oncol. Rep.* 21 (2019) 90, doi:10.1007/s11912-019-0839-6.

[2] B. Armeth, Tumor microenvironment, *Medicina* 56 (2019) 15, doi:10.3390/medicina56010015.

- [3] V. Mohan, A. Das, I. Sagi, Emerging roles of ECM remodeling processes in cancer, *Semin. Cancer Biol.* 62 (2020) 192–200, doi:10.1016/j.semcancer.2019.09.004.
- [4] S. D'Agostino, L. Tombolan, M. Saggiaro, C. Frasson, E. Rampazzo, S. Pellegrini, F. Favaretto, C. Biz, P. Ruggieri, P. Gamba, P. Bonvini, S. Aveic, R. Giovannoni, M. Pozzobon, Rhabdomyosarcoma cells produce their own extracellular matrix with minimal involvement of cancer-associated fibroblasts: a preliminary study, *Front. Oncol.* 10 (2021), doi:10.3389/fonc.2020.600980.
- [5] M. Saggiaro, E. D'Angelo, G. Bisogno, M. Agostini, M. Pozzobon, Carcinoma and sarcoma microenvironment at a glance: where we are, *Front. Oncol.* 10 (2020) 1–9, doi:10.3389/fonc.2020.00076.
- [6] V.P. Kashi, M.E. Hatley, R.L. Galindo, Probing for a deeper understanding of rhabdomyosarcoma: insights from complementary model systems, *Nat. Rev. Cancer* 15 (2015) 426–439, doi:10.1038/nrc3961.
- [7] D.S. Reynolds, K.M. Tevis, W.A. Blessing, Y.L. Colson, M.H. Zaman, M.W. Grinstaff, Breast cancer spheroids reveal a differential cancer stem cell response to chemotherapeutic treatment, *Sci. Rep.* 7 (2017) 10382, doi:10.1038/s41598-017-10863-4.
- [8] G.M. Jowett, M.D.A. Norman, T.T.L. Yu, P. Rosell Arévalo, D. Hoogland, S.T. Lust, E. Read, E. Hamrud, N.J. Walters, U. Niazi, M.W.H. Chung, D. Marciano, O.S. Omer, T. Zabinski, D. Danovi, G.M. Lord, J. Hilborn, N.D. Evans, C.A. Dreiss, L. Bozec, O.P. Oommen, C.D. Lorenz, R.M.P. da Silva, J.F. Neves, E. Gentleman, ILC1 drive intestinal epithelial and matrix remodelling, *Nat. Mater.* 20 (2021) 250–259, doi:10.1038/s41563-020-0783-8.
- [9] X. Lian, J.S. Bond, N. Bharathy, S.P. Boudko, E. Pokidysheva, J.F. Shem, M. Lathara, T. Sasaki, T. Settelmeyer, M.M. Cleary, A. Bajwa, G. Srinivasa, C.P. Hartley, H.P. Bächinger, A. Mansoor, S.H. Gultekin, N.E. Berlow, C. Keller, Defining the extracellular matrix of rhabdomyosarcoma, *Front. Oncol.* 11 (2021) 38, doi:10.3389/fonc.2021.601957.
- [10] M. Saggiaro, S. D'Agostino, A. Gallo, S. Crotti, S. D'Aronco, D. Corallo, G. Veltri, G. Martinez, A. Grigoletto, A.M. Tolomeo, G. Tafuro, M. Agostini, S. Aveic, V. Serafin, A. Semenzato, G. Pasut, M. Pozzobon, A rhabdomyosarcoma hydrogel model to unveil cell-extracellular matrix interactions, *Biomater. Sci.* 10 (2022) 124–137, doi:10.1039/D1BM00929J.
- [11] C. Chen, F. Loe, A. Blocki, Y. Peng, M. Raghunath, Applying macromolecular crowding to enhance extracellular matrix deposition and its remodeling in vitro for tissue engineering and cell-based therapies, *Adv. Drug Deliv. Rev.* 63 (2011) 277–290, doi:10.1016/j.addr.2011.03.003.
- [12] M.A. Chapman, R. Meza, R.L. Lieber, Skeletal muscle fibroblasts in health and disease, *Differentiation* 92 (2016) 108–115, doi:10.1016/j.diff.2016.05.007.
- [13] M. Raghunath, D.I. Zeugolis, Transforming eukaryotic cell culture with macromolecular crowding, *Trends Biochem. Sci.* 46 (2021) 805–811, doi:10.1016/j.tibs.2021.04.006.
- [14] Y.S. Zhang, K. Yue, J. Aleman, K. Mollazadeh-Moghaddam, S.M. Bakht, J. Yang, W. Jia, V. Dell'Erba, P. Assawes, S.R. Shin, M.R. Dokmeci, R. Oklu, A. Khademhosseini, 3D bioprinting for tissue and organ fabrication, *Ann. Biomed. Eng.* 45 (2017) 148–163, doi:10.1007/s10439-016-1612-8.
- [15] M.A. Heinrich, W. Liu, A. Jimenez, J. Yang, A. Akpek, X. Liu, Q. Pi, X. Mu, N. Hu, R.M. Schiffelers, J. Prakash, J. Xie, Y.S. Zhang, 3D bioprinting: from benches to translational applications, *Small* 15 (2019) 1–47, doi:10.1002/smll.201805510.
- [16] E.M. Langer, B.L. Allen-Petersen, S.M. King, N.D. Kendsersky, M.A. Turnidge, G.M. Kuziel, R. Riggers, R. Samatham, T.S. Amery, S.L. Jacques, B.C. Sheppard, J.E. Korkola, J.L. Muschler, G. Thibault, Y.H. Chang, J.W. Gray, S.C. Presnell, D.G. Nguyen, R.C. Sears, Modeling tumor phenotypes in vitro with three-dimensional bioprinting, *Cell Rep.* 26 (2019) 608–623 e6, doi:10.1016/j.celrep.2018.12.090.


J. Groll, J.A. Burdick, D.W. Cho, B. Derby, M. Gelinsky, S.C. Heilshorn, T. Jüngst, J. Malda, V.A. Mironov, K. Nakayama, A. Ovsianikov, W. Sun, S. Takeuchi, J.J. Yoo, T.B.F. Woodfield, A definition of bioinks and their distinction from biomaterial inks, *Biofabrication* 11 (2019), doi:10.1088/1758-5090/AAEC52.

- [18] P.S. Gungor-Ozkerim, I. Inci, Y.S. Zhang, A. Khademhosseini, M.R. Dokmeci, Bioinks for 3D bioprinting: an overview, *Biomater. Sci.* 6 (2018) 915–946, doi:10.1039/C7BM00765E.
- [19] M. Rimann, E. Bono, H. Annaheim, M. Bleisch, U. Graf-Hausner, Standardized 3D bioprinting of soft tissue models with human primary cells, *J. Lab. Autom.* 21 (2016) 496–509, doi:10.1177/2211068214567146.
- [20] S. Laternser, H. Keller, O. Leupin, M. Rausch, U. Graf-Hausner, M. Rimann, A novel microplate 3D bioprinting platform for the engineering of muscle and tendon tissues, *SLAS Technol. Transl. Life Sci. Innov.* 23 (2018) 599–613, doi:10.1177/2472630318776594.
- [21] A. Alave Reyes-Furrer, S. De Andrade, D. Bachmann, H. Jeker, M. Steinmann, N. Accart, A. Dunbar, M. Rausch, E. Bono, M. Rimann, H. Keller, Matrigel 3D bioprinting of contractile human skeletal muscle models recapitulating exercise and pharmacological responses, *Commun. Biol.* 4 (2021) 1183, doi:10.1038/s42003-021-02691-0.
- [22] J. Schindelin, I. Arganda-Carreras, E. Frise, V. Kaynig, M. Longair, T. Pietzsch, S. Preibisch, C. Rueden, S. Saalfeld, B. Schmid, J.-Y. Tinevez, D.J. White, V. Hartenstein, K. Eliceiri, P. Tomancak, A. Cardona, Fiji: an open-source platform for biological-image analysis, *Nat. Methods* 9 (2012) 676–682, doi:10.1038/nmeth.2019.
- [23] T. Ferreira, W. Rasband, ImageJ User Guide, 2012. <https://imagej.nih.gov/ij/docs/guide/146-30.html>.
- [24] J.H. Kim, Y.J. Seol, I.K. Ko, H.W. Kang, Y.K. Lee, J.J. Yoo, A. Atala, S.J. Lee, 3D bioprinted human skeletal muscle constructs for muscle function restoration, *Sci. Rep.* 81 (8) (2018) 1–15 2018, doi:10.1038/s41598-018-29968-5.
- [25] R. Saab, S.L. Spunt, S.X. Skapek, Myogenesis and rhabdomyosarcoma, *Curr. Top. Dev. Biol.*, 2011, pp. 197–234, doi:10.1016/B978-0-12-380916-2.00007-3.
- [26] M. Zanoni, M. Cortesi, A. Zamagni, C. Arienti, S. Pignatta, A. Tesi, Modeling neoplastic disease with spheroids and organoids, *J. Hematol. Oncol.* 13 (2020) 97, doi:10.1186/s13045-020-00931-0.
- [27] S. Gao, J. Shen, F. Homicek, Z. Duan, Three-dimensional (3D) culture in sarcoma research and the clinical significance, *Biofabrication* 9 (2017) 032003, doi:10.1088/1758-5090/aa7fdb.
- [28] D.M. Parham, F.G. Barr, Classification of rhabdomyosarcoma and its molecular basis, *Adv. Anat. Pathol.* 20 (2013) 387–397, doi:10.1097/PAP.0b013e3182a92d0d.
- [29] S.X. Skapek, A. Ferrari, A.A. Gupta, P.J. Lupo, E. Butler, J. Shipley, F.G. Barr, D.S. Hawkins, Rhabdomyosarcoma., *Nat. Rev. Dis. Prim.* 5 (2019) 1, doi:10.1038/s41572-018-0051-2.
- [30] A.R.P. Hinson, R. Jones, L.E.S. Crose, B.C. Belyea, F.G. Barr, C.M. Linardic, Human rhabdomyosarcoma cell lines for rhabdomyosarcoma research: utility and pitfalls, *Front. Oncol.* 3 (2013) 183, doi:10.3389/fonc.2013.00183.
- [31] F. Petragliano, I. Pietrantonio, S. Camero, S. Codenotti, L. Milazzo, F. Vulcano, G. Macloce, I. Giordani, P. Tini, S. Cheleschi, G.L. Gravina, C. Festuccia, A. Rossetti, S. Delle Monache, A. Ordinelli, C. Ciccarelli, A. Mauro, B. Barbara, C. Antinozzi, A. Schiavetti, R. Maggio, L. Di Luigi, A. Polimeni, C. Marchese, V. Tombolini, A. Fanzani, N. Bernabò, F. Megiomi, F. Marampon, Clinically relevant radioresistant rhabdomyosarcoma cell lines: functional, molecular and immune-related characterization, *J. Biomed. Sci.* 27 (2020) 1–18, doi:10.1186/S12929-020-00683-6/FIGURES/6.
- [32] M. Peron, P. Bonvini, A. Rosolen, Effect of inhibition of the Ubiquitin-Proteasome System and Hsp90 on growth and survival of Rhabdomyosarcoma cells in vitro, *BMC Cancer* 12 (2012),

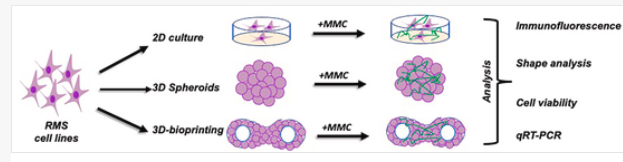
- [33] V. Masola, C. Maran, E. Tassone, A. Zin, A. Rosolen, M. Onisto, Heparanase activity in alveolar and embryonal rhabdomyosarcoma: implications for tumor invasion, *BMC Cancer* 9 (2009) 304, doi:10.1186/1471-2407-9-304.
- [34] V. Masola, C. Maran, E. Tassone, A. Zin, A. Rosolen, M. Onisto, Heparanase activity in alveolar and embryonal rhabdomyosarcoma: implications for tumor invasion, *BMC Cancer* 9 (2009) 304, doi:10.1186/1471-2407-9-304.
- [35] F. Ramadan, A. Fahs, S.E. Ghayad, R. Saab, Signaling pathways in Rhabdomyosarcoma invasion and metastasis, *Cancer Metastasis Rev.* 39 (2020) 287–301, doi:10.1007/s10555-020-09860-3.
- [36] E.R. Rudzinski, J.R. Anderson, Y.-Y. Chi, J.M. Gastier-Foster, C. Astbury, F.G. Barr, S.X. Skapek, D.S. Hawkins, B.J. Weigel, A. Pappo, W.H. Meyer, M.A. Arnold, L.A. Teot, D.M. Parham, Histology, fusion status, and outcome in metastatic rhabdomyosarcoma: a report from the Children's Oncology Group, *Pediatr. Blood Cancer* 64 (2017) e26645, doi:10.1002/pbc.26645.
- [37] P. Kumar, A. Satyam, X. Fan, E. Collin, Y. Rochev, B.J. Rodriguez, A. Gorelov, S. Dillon, L. Joshi, M. Raghunath, A. Pandit, D.I. Zeugolis, Macromolecularly crowded in vitro microenvironments accelerate the production of extracellular matrix-rich supramolecular assemblies, *Sci. Rep.* 5 (2015) 8729, doi:10.1038/srep08729.
- [38] A. Satyam, P. Kumar, X. Fan, A. Gorelov, Y. Rochev, L. Joshi, H. Peinado, D. Lyden, B. Thomas, B. Rodriguez, M. Raghunath, A. Pandit, D. Zeugolis, Macromolecular crowding meets tissue engineering by self-assembly: a paradigm shift in regenerative medicine, *Adv. Mater.* 26 (2014) 3024–3034, doi:10.1002/adma.201304428.
- [39] D. Tsiapalis, A. De Pieri, K. Spanoudes, I. Sallent, S. Kearns, J.L. Kelly, M. Raghunath, D.I. Zeugolis, The synergistic effect of low oxygen tension and macromolecular crowding in the development of extracellular matrix-rich tendon equivalents, *Biofabrication* 12 (2020) 025018, doi:10.1088/1758-5090/ab6412.
- [40] X.M. Ang, M.H.C. Lee, A. Blocki, C. Chen, L.L.S. Ong, H.H. Asada, A. Sheppard, M. Raghunath, Macromolecular crowding amplifies adipogenesis of human bone marrow-derived mesenchymal stem cells by enhancing the pro-adipogenic microenvironment, *Tissue Eng.* 20 (2014) 966–981, doi:10.1089/ten.tea.2013.0337.
- [41] M.H. Lee, A.G. Goralczyk, R. Kriszt, X.M. Ang, C. Badowski, Y. Li, S.A. Summers, S.-A. Toh, M.S. Yassin, A. Shabbir, A. Sheppard, M. Raghunath, ECM microenvironment unlocks brown adipogenic potential of adult human bone marrow-derived MSCs, *Sci. Rep.* 6 (2016) 21173, doi:10.1038/srep21173.
- [42] A.S. Zeiger, F.C. Loe, R. Li, M. Raghunath, K.J. Van Vliet, Macromolecular crowding directs extracellular matrix organization and mesenchymal stem cell behavior, *PLoS One* 7 (2012) e37904, doi:10.1371/journal.pone.0037904.
- [43] R. Rashid, S.M.L. Chee, M. Raghunath, T. Wohland, Macromolecular crowding gives rise to microviscosity, anomalous diffusion and accelerated actin polymerization, *Phys. Biol.* 12 (2015) 034001, doi:10.1088/1478-3975/12/3/034001.
- [44] O.W. Petersen, L. Rønnov-Jessen, V.M. Weaver, M.J. Bissell, Differentiation and cancer in the mammary gland: shedding light on an old dichotomy, *Adv. Cancer Res.*, *Adv Cancer Res*, 1998, pp. 135–162, doi:10.1016/S0065-230X(08)60741-1.
- [45] A. Lochter, M.J. Bissell, Involvement of extracellular matrix constituents in breast cancer, *Semin. Cancer Biol.* 6 (1995) 165–173, doi:10.1006/scbi.1995.0017.
- [46] L. Sun, J. Fang, Macromolecular crowding effect is critical for maintaining SIRT1's nuclear localization in cancer cells, *Cell Cycle* 15 (2016) 2647–2655, doi:10.1080/15384101.2016.1211214.
- [47] S. Thuault, F. Comunale, J. Hasna, M. Fortier, D. Planchon, N. Elarouci, A. De Reynies, S. Bodin, A. Blangy, C. Gauthier-Rouvière, The RhoE/ROCK/ARHGAP25 signaling pathway controls cell

invasion by inhibition of Rac activity, *Mol. Biol. Cell* 27 (2016) 2653–2661, doi:10.1091/mbc.e16-01-0041.

- [48] C. de L. Davies, D.A. Berk, A. Pluen, R.K. Jain, Comparison of IgG diffusion and extracellular matrix composition in rhabdomyosarcomas grown in mice versus in vitro as spheroids reveals the role of host stromal cells, *Br. J. Cancer* 86 (2002) 1639–1644, doi:10.1038/sj.bjc.6600270.
- [49] T. Liu, C. Delavaux, Y.S. Zhang, 3D bioprinting for oncology applications, *J. 3D Print. Med.* 3 (2019) 55–58, doi:10.2217/3dp-2019-0004.
- [50] Y.S. Zhang, M. Duchamp, R. Oklu, L.W. Ellisen, R. Langer, A. Khademhosseini, Bioprinting the cancer microenvironment, *ACS Biomater. Sci. Eng.* 2 (2016) 1710–1721, doi:10.1021/acsbiomaterials.6b00246.
- [51] J.L. Albritton, J.S. Miller, 3D bioprinting: improving in vitro models of metastasis with heterogeneous tumor microenvironments, *Dis. Model. Mech.* 10 (2017) 3–14, doi:10.1242/dmm.025049.
- [52] J. Munoz-Garcia, C. Jubelin, A. Loussouarn, M. Goumard, L. Griscom, A. Renodon-Cornière, M.-F. Heymann, D. Heymann, In vitro three-dimensional cell cultures for bone sarcomas, *J. Bone Oncol.* 30 (2021) 100379, doi:10.1016/j.jbo.2021.100379.
- [53] G. Bahcecioglu, G. Basara, B.W. Ellis, X. Ren, P. Zorlutuna, Breast cancer models: engineering the tumor microenvironment, *Acta Biomater.* 106 (2020) 1–21, doi:10.1016/j.actbio.2020.02.006.
- [54] R. Gómez-Oliva, S. Domínguez-García, L. Carrascal, J. Abalos-Martínez, R. Pardillo-Díaz, C. Verástegui, C. Castro, P. Nunez-Abades, N. Geribaldi-Doldán, Evolution of experimental models in the study of glioblastoma: toward finding efficient treatments, *Front. Oncol.* 10 (2021) 3245, doi:10.3389/fonc.2020.614295.
- [55] M. Tang, J.N. Rich, S. Chen, Biomaterials and 3D bioprinting strategies to model glioblastoma and the blood–brain barrier, *Adv. Mater.* 33 (2021) 2004776, doi:10.1002/adma.202004776.
- [56] X. Wang, X. Li, Y. Zhang, X. Long, H. Zhang, T. Xu, C. Niu, Coaxially bioprinted cell-laden tubular-like structure for studying glioma angiogenesis, *Front. Bioeng. Biotechnol.* 9 (2021) 761861, doi:10.3389/fbioe.2021.761861.
- [57] Katja Hölzl, 7 Shengmao Lin^{3,6}, 5 Liesbeth Tytgat⁴, 5 Sandra Van Vlierberghe⁴, Linxia Gu³, 2 Aleksandr Ovsianikov¹, Bioink properties before, during and after 3D bioprinting, *Biofabrication* 8 (2016).
- [58] S.M. Hull, L.G. Brunel, S.C. Heilshorn, 3D bioprinting of cell-laden hydrogels for improved biological functionality, *Adv. Mater.* (2021) 2103691, doi:10.1002/adma.202103691.
- [59] J. Zhang, E. Wehrle, M. Rubert, R. Müller, 3D bioprinting of human tissues: biofabrication, bioinks, and bioreactors, *Int. J. Mol. Sci.* 22 (2021) 3971, doi:10.3390/ijms22083971.
- [60] J. Libura, J. Drukala, M. Majka, O. Tomescu, J.M. Navenot, M. Kucia, L. Marquez, S.C. Peiper, F.G. Barr, A. Janowska-Wieczorek, M.Z. Ratajczak, CXCR4–SDF-1 signaling is active in rhabdomyosarcoma cells and regulates locomotion, chemotaxis, and adhesion, *Blood* 100 (2002) 2597–2606, doi:10.1182/blood-2002-01-0031.
- [61] L. Xu, R. Tong, D.M. Cochran, R.K. Jain, Blocking platelet-derived growth factor-D/platelet-derived growth factor receptor β signaling inhibits human renal cell carcinoma progression in an orthotopic mouse model, *Cancer Res.* 65 (2005) 5711–5719, doi:10.1158/0008-5472.CAN-04-4313.

 Images are optimised for fast web viewing. Click on the image to view the original version.

alt-text: Image 1



Appendix A Supplementary data

The following is the Supplementary data to this article:

 [Multimedia Component 1](#)

Fig. S1

Immunofluorescence staining for collagen I (COLI), laminin (LAM) and fibronectin (FN) in RH30 (ARMS) (**left**) and RD (ERMS) (**right**) xenogenic samples. Cell nuclei are counterstained with DAPI. N = 4. Scale bar = 50 μ m.

alt-text: Fig. S1

Queries and Answers

Q1

Query: Please confirm that the provided **emails** “ragh@zhaw.ch, michela.pozzobon@unipd.it” are the correct address for official communication, else provide an alternate e-mail address to replace the existing one, because private e-mail addresses should not be used in articles as the address for communication.

Answer: Reviewed

Q2

Query: Have we correctly interpreted the following funding source(s) and country names you cited in your article: Department of Women and Children Health; University of Padova; Institute of Pediatric research Città della Speranza (IRP); EU COST; Institute of Pediatric Research Città della Speranza.?

Answer: yes, all good